THE BALTIC JOURNAL
OF ROAD
AND BRIDGE
ENGINEERING
2023/18(2)

ISSN 1822-427X/eISSN 1822-4288
2023 Volume 18 Issue 2: 152–189
https://doi.org/10.7250/bjrbe.2023-18.602

EXPERIMENTAL INVESTIGATION OF THE BEARING PERFORMANCE AND FAILURE CHARACTERISTICS OF DOUBLE-ROW PILE-SLAB STRUCTURES IN STEEP MOUNTAINOUS AREAS

RUI SU, QIAN SU*, PENG CHENG, HENG ZHOU, XUN WANG, YANFEI PEI

Southwest Jiaotong University, Chengdu 610031, China

Received 8 May 2022; accepted 13 March 2023

Abstract. Considering the pile-slab subgrade project of the Hangzhou-Huang Shan Passenger Dedicated Line as the basis, this paper conducts a 1:10 large-scale indoor model test for the horizontal bearing capacity of the pile-slab structure in steep mountainous areas to study the distribution of the pile-slab structure stress, soil pressure and structural deformation and analyze the failure mode of the structure and slope. The research shows that when the subgrade with a double-row pile-slab structure is subjected to horizontal loading in the steep slope section, the steel bars of the pile body above the sliding surface are compressed, and the steel bars of the pile body below the sliding surface are under tension. With the increase in the horizontal load, the stress of the pile body steel bar remains basically unchanged or shows a steady increase and finally sharply increases. The deformation of the bearing plate is

* Corresponding author. E-mail: suqian@126.com

Rui SU (ORCID ID 0009-0005-3411-537X)
Qian SU (ORCID ID 0009-0007-8260-0016)
Peng CHENG (ORCID ID 0009-0002-5985-3836)
Heng ZHOU (ORCID ID 0009-0004-9929-1000)
Xun WANG (ORCID ID 0000-0001-5878-423X)
Yanfei PEI (ORCID ID 0009-0000-3723-0051)

dominated by the horizontal displacement, and the horizontal displacement reaches 7.25 mm when the plate is broken. In addition, warping deformation of the inner high and outer low occurs. When the horizontal load reaches 157 kN, shallow damage and local collapse of the slope occur, and transverse and diagonal cracks occur at the top of the pile and near the sliding surface of the pile. During the test, the pile-slab structure always deforms more than the slope, and the overall stability of the structure is good. The test is suitable for sections where the remaining sliding force is less than 770 kN/m (equivalent to a slope length of 79.123 m).

Keywords: bearing performance, failure characteristic, high-speed railway subgrade, indoor model test, pile-slab structure, steep slope.

Introduction

Pile-slab structures have been widely used in various projects, e.g., in construction of high-speed railways (Jiang et al., 2014; Zhang et al., 2018), highways (Chau et al., 2012), airport (Zhou et al., 2021) and emergency engineering (Kahyaoglu et al., 2017) projects due to many advantages they offer, such as strong anti-skid ability, small amount of masonry, flexible pile layout, convenient construction, and small construction influence range. Pile-slab structures can help effectively overcome various technical problems, such as soft soil roadbeds (Zhang et al., 2018), high-filled roadbed slopes (Zhu et al., 2020), and landslides (Xiao et al., 2017; Guo et al., 2019; Gao et al., 2020; Zhu et al., 2020; Xie et al., 2021). The pile-slab structure originates from the anti-slide pile, but it has a different force mechanism as compared to the anti-slide pile. Therefore, the engineering community has been working on these two types of subgrade support structures. Regarding their different force characteristics, pile slab roadbeds are mainly classified into load-bearing pile slab roadbeds and load-bearing support pile slab roadbeds. Load-bearing pile slab roadbed can be regarded as an alternative structure for foundation reinforcement or stiffness transition measures; the pile slab structure transfers the upper vertical load to the deeper stable soil layer, the pile body mainly relies on the side friction and pile end bearing effect to support the upper load, the pile slab structure and the roadbed filling act together to form a load-bearing structure system. The load-bearing support pile slab structure and the bedrock are wrapped together to form a composite structure, the bearing mechanism is complex, which not only poses the problem of structural bearing capacity, but also the bearing capacity of the rock and soil. At the same time, the problems related to the bearing capacity of the geotechnical body and the plate-soil, pile-soil interaction also emerge, therefore, it is necessary to carry out in-depth research. The double-row pile-plate structure is a load-bearing support type pile-plate structure, which is more suitable for the steep slope than the traditional pile-plate structure.

Many scholars have conducted in-depth studies on slope stability and reinforcement methods (Galli & di Prisco, 2013; Di Laora et al., 2017; Troncone et al., 2021). Salah studied the dynamic response of pile-slab structures under different cushion materials through investigations and numerical calculations of pile-slab structures. It was noted that the material properties of the cushion greatly affect the horizontal and vertical dynamic impedance of the structure (Messioud et al., 2016; Messioud et al., 2017). Ravera et al. proposed a finite element calculation method to calculate the pile-soil-slab interaction (Ravera et al., 2020). Wei conducted on-site driving tests and dynamic calculations on the pile-slab structure roadbed of the bridge-tunnel transition section and suggested that the structure had good dynamic performance, and the design of a variable pile length was beneficial to the smooth transition of the stiffness of the transition section (Li et al., 2020a; Wei et al., 2020). Su performed on-site vibration tests on the low subgrade of a ballastless track supported by a pile-slab structure, which proved that the structure had good long-term dynamic stability (Huang et al., 2015). Li proposed a simplified model of slope stability analysis for double-row pile reinforcement (Li et al., 2020b). Li, Lei, and Gang performed large-scale shaking table tests and numerical calculations and concluded that the best position for double-row pile reinforcement was the middle and lower parts of the slope (Fan et al., 2019; Li et al., 2020b; Lei et al., 2021). Wang proposed a calculation method to determine the optimal time interval to construct the front and rear piles of a double-row pile-slab structure, considering design safety, cost, and stability as calculation parameters (Wang et al., 2020). Zhou and others performed large-scale physical model tests to simulate the deformation of double-row piles during the excavation of deep foundation pits (Zhou et al., 2016). The soil pressure is higher around the front row of piles than around the back row of piles. The distribution of soil pressure around the front row of piles is “right convex”, and the soil pressure of the back row of piles significantly changes at the pile-soil interface. Buslov and Margolin investigated 4000 double-row pile structures with different design parameters and summarized the evaluation method for the effective utilization rate of the second row of piles (Buslov & Margolin, 2017; Buslov & Margolin, 2018).

Nowadays, a large number of high-speed railways are constructed in mountainous areas. In contrast to traditional pile-slab structures, the use of double-row pile slab structures in steep sections of such projects can reduce the number of the required bridges and tunnels to be built, effectively reduce project costs, improve project schedule, and facilitate rapid repair of *force majeure* damage, such as damage caused by earthquakes. In addition to the vertical load, the double-row pile-slab structure subgrade in the steep slope section also bears the horizontal load generated by own weight of the upper slope, which leads to lateral deformation of the structure, instability and destruction. The current numerical simulation technology cannot comprehensively simulate the damage characteristics of double-row pile plate structures in high and steep slope engineering applications. Therefore, a large-scale indoor test study was performed to analyze the horizontal bearing performance, structural deformation characteristics, and subgrade failure characteristics of the double-row pile-slab structure subgrade. This test is currently the largest indoor model test of pile-slab structures, which may have significant implications for design and application of such structures in future.

1. Project overview

Hang-Huang high-speed railway connects Zhejiang and Anhui provinces, as shown in Figure 1. It is of great significance to the development and improvement of the Chinese railway network and economic development. Hang-Huang Railway has a total length of 287 km and a design speed of 250 km/h. It is a double-track railway that crosses many unfavorable geological zones. The geological conditions along the line are relatively complex. There are 87 tunnels, 1 extra-large bridge, and 3 subgrade sections.

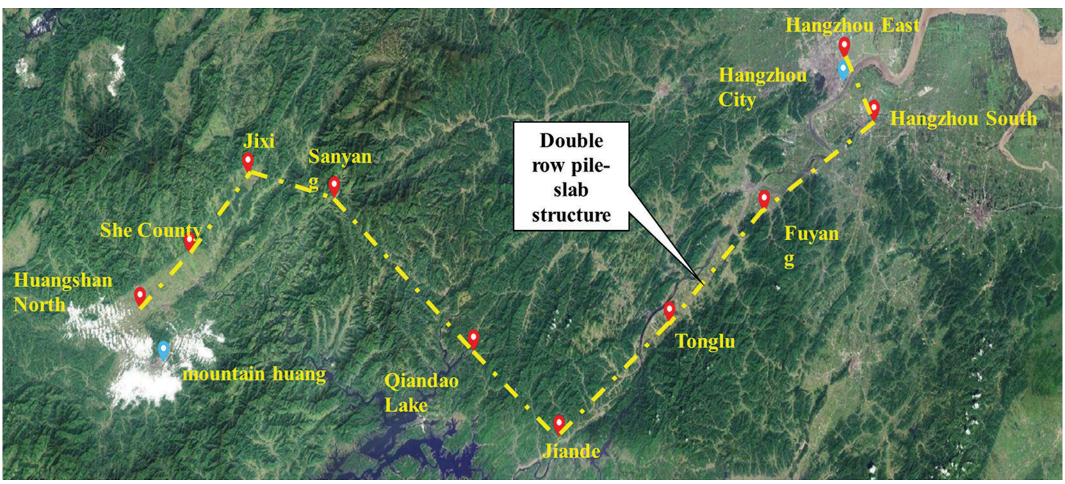

Figure 1. Schematic diagram of Hang-Huang Railway

The double-row pile-slab structure of the short-circuit foundation between bridges and tunnels is considered as the research object in this paper. The subgrade of the steep slope section between the bridge and tunnel is approximately 28.5 m long, accounting for 1/5 of the total length of the subgrade. It is located in denuded hilly areas and valleys between the hills. The vegetation basically consists of low bushes, the terrain is undulating, and the natural slope of the mountain is approximately 25°–40°. The valley between the hills is flat and opened up for farmland. The geological conditions include an overlying layer of silty clay (2–3 m), a middle layer of fully weathered and strongly weathered mudstone (5–6 m), and a bottom layer of weakly weathered mudstone. The slope is filled with AB or C group fillers (Group A fillers are good quality fillers, including hard stones, well-graded and fine-grained soils with less than 15% drift stone, pebble soils, gravelly soils, round gravelly soils, angular gravelly soils, gravelly sands, coarse sands, and medium sands. Group B fillers are good aggregates, including soft stones that are not easily weathered, driftstone soil, pebble soil, gravelly soil, round gravelly soil, angular gravelly soil, gravelly sand, coarse sand and medium sand with a fine-grained soil content of 15% to 30%. Group C fillers are general fills, including soft boulders that are easily weathered, driftstone soils with a fine soil content of 30% or more, pebble soils, gravelly soils, round gravelly soils, angular gravelly soils, gravelly sands, coarse sands and medium sands). The physical and mechanical parameters of strongly weathered mudstone, weakly weathered mudstone, and roadbed filler were tested at the construction site. The results are shown in Table 1.

Due to the large undulations and complicated geological conditions, it was difficult to fully reproduce the original appearance of the steep

Table 1. Physical and mechanical parameters of the soil at the engineering site

Term	Density, kg/m^3	Dry density, kg/m^3	Compressive strength, MPa	Elastic modulus, MPa	Moisture capacity	Degree of compaction	Cohesion, kPa	Internal friction angle, °
Strong weathered mudstone	2100		16	490	–	–	55	28
Weak weathered mudstone	2200		25	750	–	–	200	32
Roadbed fillings	1900	1681	–	–	13%	90%	25	20

a) Transverse section view

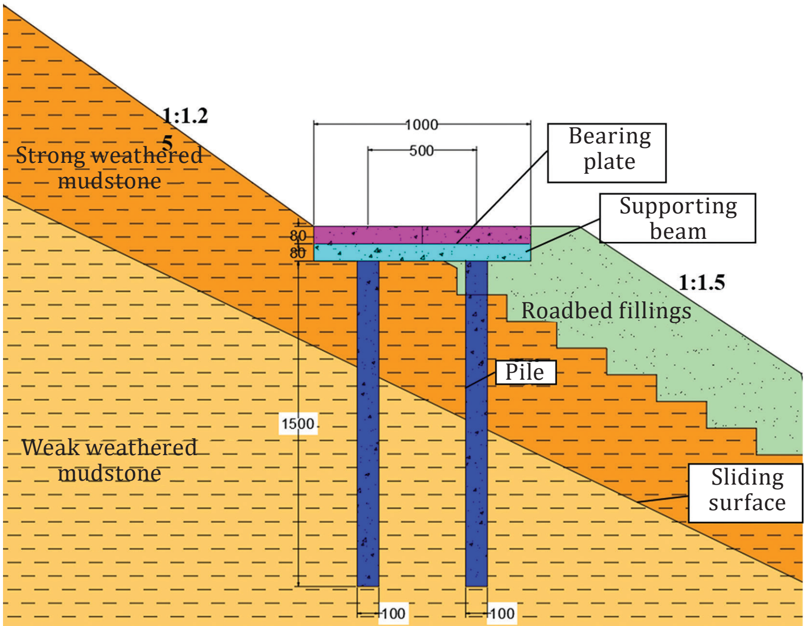

b) Longitudinal section view

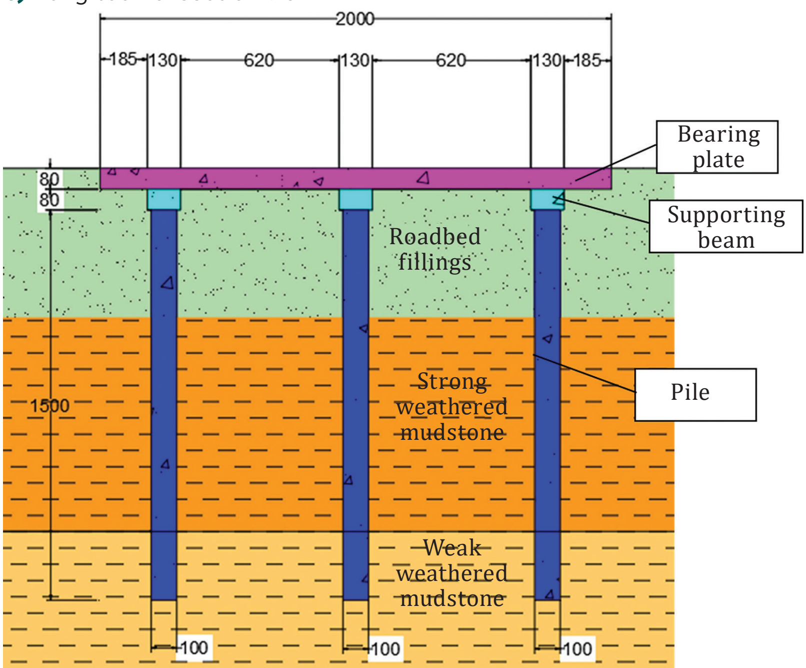

Figure 2. Schematic diagram of the feature section (unit: cm)

slope section of the bridge and tunnel in the model test, and it was necessary to select characteristic sections for analysis. According to the geological survey data, the interface between strong weathered mudstone and weak weathered mudstone at section DK106+340 has the largest inclination angle of 34.09°, and the upper part of the structure has a steep slope of 1:1.25, which is the steepest slope of domestic roadbed engineering at present, as shown in Figure 2. Therefore, this section has the highest potential to cause damage to the subgrade pile structure. For this reason, it was selected as the characteristic section to conduct the test.

2. Indoor large-scale model test design

The double-row pile-slab structure is a new type of foundation. It is rarely used in the steep slopes of mountainous areas in China, and limited research data are available. The analysis of the damage characteristics of the pile-slab structure involves the interaction between the soil and the structure, the numerical and theoretical methods could not be adopted without the verification of indoor model test since material parameters and contact relationship are complex. Therefore, it was necessary to use indoor model tests to study double-row pile-slab structures.

2.1. Model size and similarity ratio design

Under static loading, expressions of stress and displacement of the pile-slab structure are shown in Equations (1) and (2) (Xv, 1982).

$$\sigma = f\left(F, q, \gamma, l, E, \upsilon, p\right) \tag{1}$$

$$S = f\left(F, q, \gamma, l, E, \upsilon, p\right) \tag{2}$$

where F is the concentrated load; q is the line load; γ is the unit weight; l is the structure size; E is the elastic modulus of the material; and p is the ratio of reinforcement.

Through dimensional analysis (Xv, 1982), Equation (3) is obtained.

$$\left[\sigma\right] = \left[Fl^{-2} \cdot \left(\frac{ql}{F}\right)^{b} \cdot \left(\frac{\gamma l^{3}}{F}\right)^{c} \cdot \left(\frac{El^{2}}{F}\right)^{e} \cdot \upsilon^{f} \cdot p^{g}\right] \tag{3}$$

Then, the similarity criterion is obtained, as shown in Equation (4).

$$\pi_1 = p, \pi_2 = \upsilon, \pi_3 = \frac{El^2}{F}, \pi_4 = \frac{\gamma l^3}{F}, \pi_5 = \frac{ql}{F}, \pi_6 = \frac{\sigma l^2}{F}, \pi_7 = \frac{SEl}{F} \tag{4}$$

Taking the actual engineering project as the basis, this experiment will scale down the engineering prototype by 1:10 and use similar materials. In the model test, the geometric similarity ratio between the model and the prototype is 1:10, the elastic modulus similarity ratio is 1:1, and the Poisson ratio similarity ratio is 1:1. The similarity relationship of the model test is mainly ensured with regard to the geometric dimensions of the pile-slab structure and pile-slab elastic

Table 2. Model test similarity constant (model/prototype)

Term	Symbol	Similarity constant	Term	Symbol	Similarity constant
Length (L)	C_l	1/10	Stress ($ML^{-1}T^{-2}$)	C_δ	1
Density (ML^{-3})	C_ρ	1	Strain (-)	C_ε	1
Elastic Modulus ($ML^{-1}T^{-2}$)	C_E	1	Concentrate load (MLT^{-2})	C_F	1/100
Poisson ratio (–)	C_υ	1	Unit weight ($ML^{-2}T^{-2}$)	C_γ	1
Internal friction angle (–)	C_C	1	Reinforcement ratio (–)	C_P	1

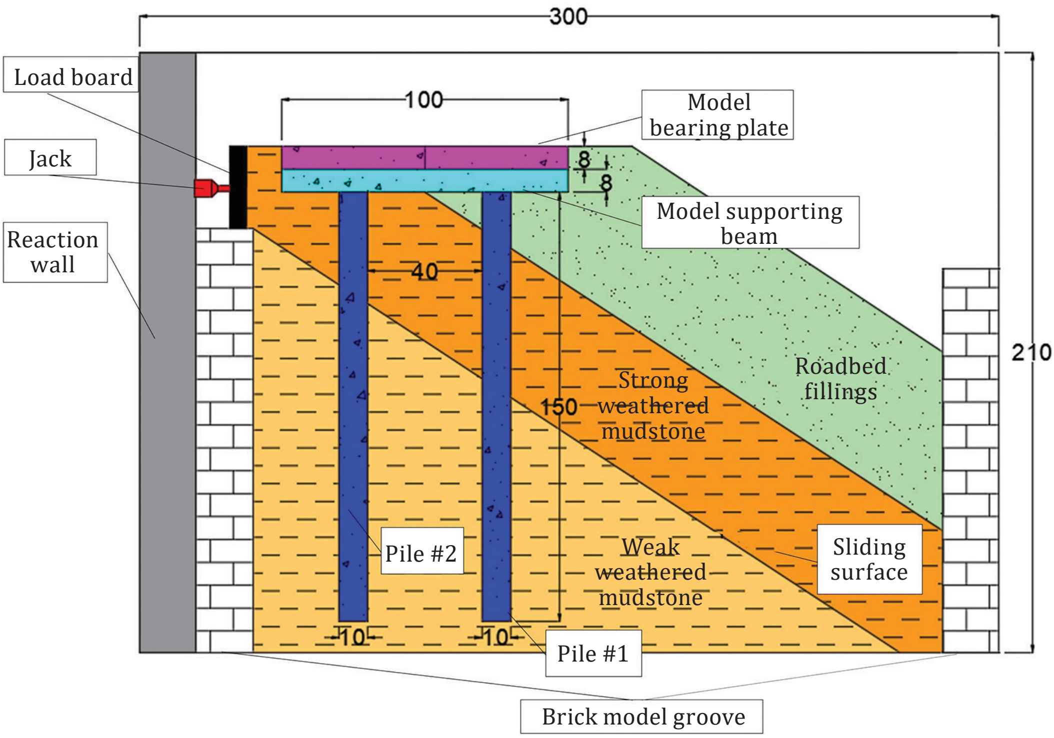

Figure 3. Schematic diagram of the model layout (unit: cm)

modulus. The test model is made from the same material as the prototype, although criterion π_4 (Xv, 1982) cannot be satisfied. This test mainly explores the internal force changes and deformations of various components of the pile-slab structure. The stress and displacement caused by their own weight are not the focus of this research; hence, this requirement can be partially dismissed. To compensate for the lack of bulk density, the form of external force is added to the model to ensure that the stress generated by the control section is equivalent. Following the π theorem (Xv, 1982), i.e., E. Buckingham's theorem, similar constants of other physical and mechanical parameters are given in Table 2.

To ensure that the structure of the indoor model is close to the actual project, the model takes 3 times the length of the board along the line and 3 times the width along the line. Therefore, with regard to the geometric similarity ratio of the model, the size of the model chamber is determined to be 2.5 m in length, 3 m in width and 2.5 m in height. The layout of the model is shown in Figure 3. Before filling, a sufficient amount of petroleum jelly was applied on the inside of the model groove to reduce the influence of the boundary on the model.

2.2. Materials and mechanical parameters of the model

This model is composed of the pile-slab structure, bedrock, and roadbed fillings.

Pile-slab structure model

Microaggregate reinforced concrete was used to simulate reinforced concrete. Indoor tests were carried out according to ASTM C39 (ASTM C39/39M-18). During the test, the microaggregate reinforced concrete was sieved into aggregates of various particle sizes. Then, the mix proportion of the microaggregate reinforced concrete in the test was determined according to the site grade of the concrete.

The requirements of similarity should be satisfied with regard to the material properties, such as the yield strength, ultimate strength, elastic modulus, and stress-strain curve shape of the steel bars in the pile-slab structure. Therefore, a steel wire with a diameter of 4 mm was selected to simulate the steel bar in the test (to easily paste the strain gauge, a thin steel sheet was used to simulate the steel bar in the internal force test), and wire cutters were used to indent the surface of the steel wire to simulate the actual bond between the steel bar and the concrete. Table 3 presents the laboratory test results for microaggregate reinforced concrete.

Table 3. Physical and mechanical parameters of microaggregate reinforced concrete

Part	Material	Unit weight, kg/m^3	Elastic modulus, MPa	Compressive strength, MPa	Poisson ratio
Pile	microaggregate reinforced concrete	2350	27 600	36.2	0.2
Bearing plate	microaggregate reinforced concrete	2350	27 600	36.2	0.2
Supporting beam	microaggregate reinforced concrete	2350	27 600	36.2	0.2

Bedrock model

According to a similar relationship, a mixture of clay, gypsum, cement, sand, and water was selected to simulate mudstone. The physical and mechanical parameters of the prototype mudstone are given in Table 1. According to (ASTM C39/39M-18), the uniaxial compressive strength and elastic modulus of the mixture with different proportions were tested; the test results are presented in Table 4. Substituting the mechanical parameters of the mixture with different proportions and the prototype parameters in the similarity criterion, it was concluded that the third group could simulate strongly weathered mudstone and the fourth group could simulate weakly weathered mudstone.

Table 4. Mix proportion test result

Group	Proportion, %					Density, kg/m^3	Uniaxial compressive strength, MPa	Elastic Modulus, MPa
	Clay	Gypsum	Cement	Water	Sand			
1	64.42	7.36	11.76	8.79	7.67	2106	1.9	630
2	68.16	7.01	10.22	7.30	7.30	2052	1.8	590
3	70.78	6.53	8.62	7.26	6.81	2020	1.6	500
4	68.36	5.26	10.08	7.54	8.76	2080	2.4	720
5	64.62	6.15	10.77	8.21	10.26	2052	2.1	680
6	67.96	5.83	9.22	7.28	9.71	2058	1.6	530

Roadbed fillings

In the model test, it was difficult to scale the size of soil particles according to a similar ratio. To eliminate the influence of the size of soil particles on the test, clay with a particle size of less than 2 mm was used to simulate roadbed fillings. To ensure that the model filler and actual roadbed filler can meet similar criteria $c_\rho \approx 1$, according to (GB/T50123-2019), basic physical experiments, such as drying,

Table 5. Physical properties of test clay

Parameter	Maximum dry density, kg/m^3	Dry density, kg/m^3	Cohesion, kPa	Internal friction angle, °
Value	2100	1653	25	20

Figure 4. Compaction test

compaction, and triaxial test were performed, as shown in Figure 4. Test results are given in Table 5. The results show that the filler in the experiment could simulate the actual roadbed filler as used within the project. Thirteen percent of the water volume and 90% of compaction were used as model filling quality control indicators.

2.3. Test preparation procedure

The preparation procedure is divided into the following three steps:

Binding steel cage of model piles, bearing plates and supporting beam, precast model piles

The number of rows and reinforcement ratios of the model main bars were consistent with those of the main bars of the prototype. The spacing between the structural ribs of the model was reduced according to the model scale. After the steel cage was tied (Figure 5), strain gauges were pasted on it, and the model piles were poured after erecting the mold and then cured for approximately 7 days.

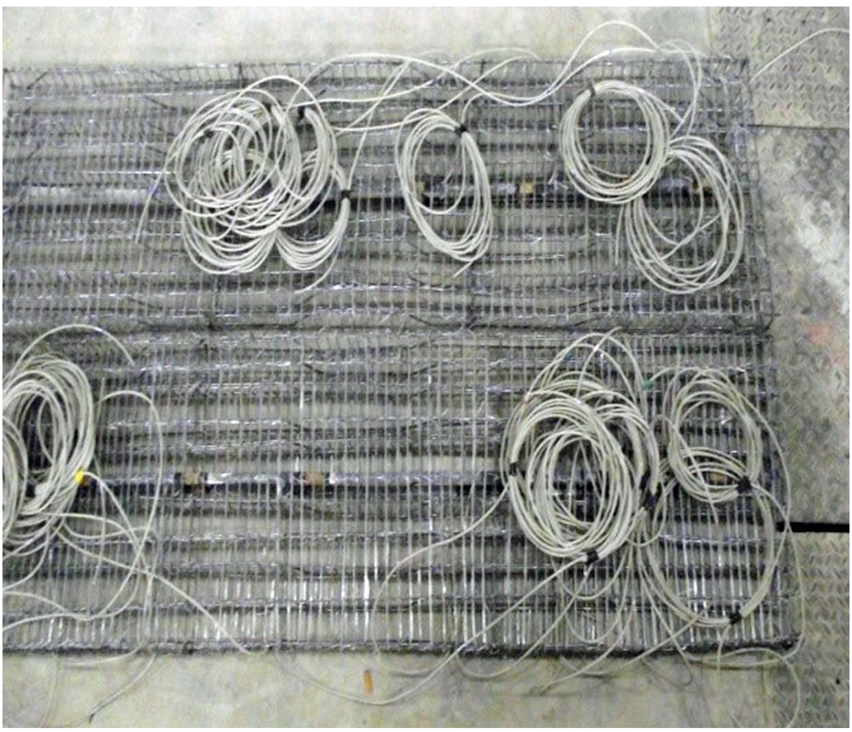

Figure 5. Steel cage of the bearing plates of the model

Masonry model groove and fill soil

The model groove was made of bricks in the laboratory, and sandbags were piled around the model groove to prevent the model tank from being deformed or collapsing. The bedrock model was filled in the model groove. Then, the earth pressure cell was buried at the bottom of the pile. Afterwards, the model piles were erected (Figure 6), and the soil was filled in layers, with each layer less than 10 cm below the top of the model piles (Figure 7). In addition, when filling, the surface of the fill at the interface, open pits, etc., had to be shaved to strengthen the friction between each layer of fill. During the filling process, the earth pressure cell was buried according to the design.

On-site pouring of the bearing plate and supporting beam structure model

When filling the top surface of the pile foundation with soil, the formwork of the bearing plate and supporting beam was erected (Figure 8). Next, the steel cage of the slab and the beam were placed, the concrete was poured in steps, and curing was allowed for 3 days before the next step of pouring.

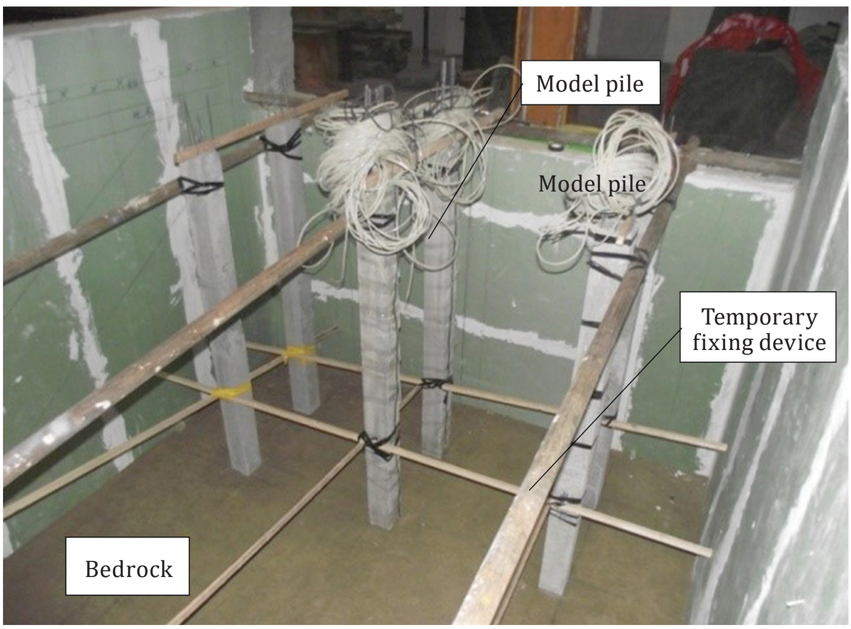

Figure 6. Erecting model piles

Figure 7. Filling soil

Figure 8. Erecting the formwork of the bearing plate

2.4. Measurement scheme

The purpose of this test is to explore stress distribution, deformation characteristics and failure characteristics of the pile-slab structure applied to the steep slope section. Therefore, in this model test, resistance strain gauges were arranged at different parts of the pile-slab

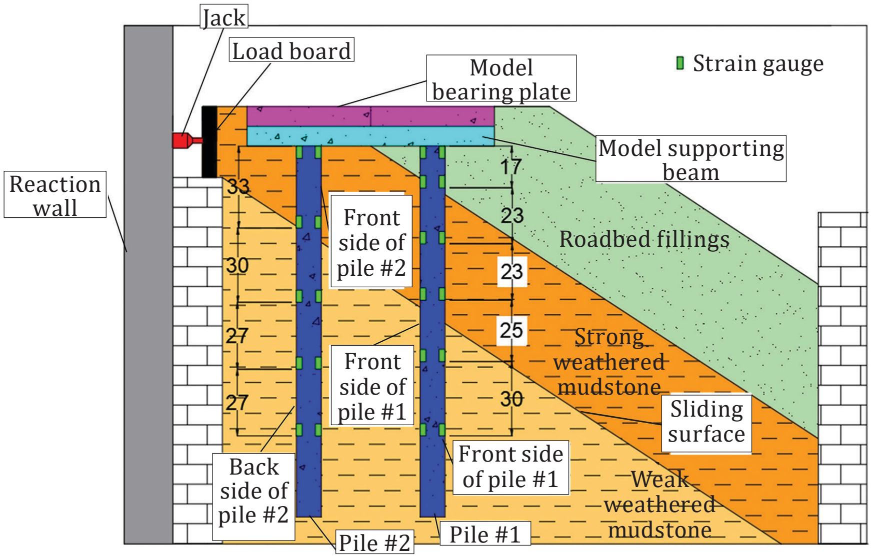

Figure 9. Strain measuring point layout (unit: cm)

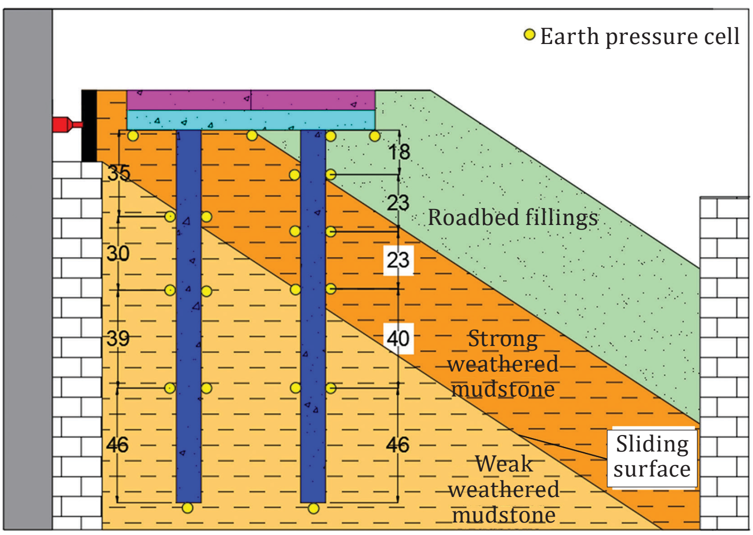

Figure 10. Earth pressure measuring point layout (unit: cm)

structure to collect the internal force of the structure; the specific positions are shown in Figure 9. Micro earth pressure cells with a range of 200 kPa were buried along the piles at different depths to obtain the data on the distribution of earth pressures along the pile depth. The specific burying positions are shown in Figure 10. Dial indicators with an accuracy of 0.01 mm were used to monitor the roadbed deformation. The specific placement position is shown in Figure 11.

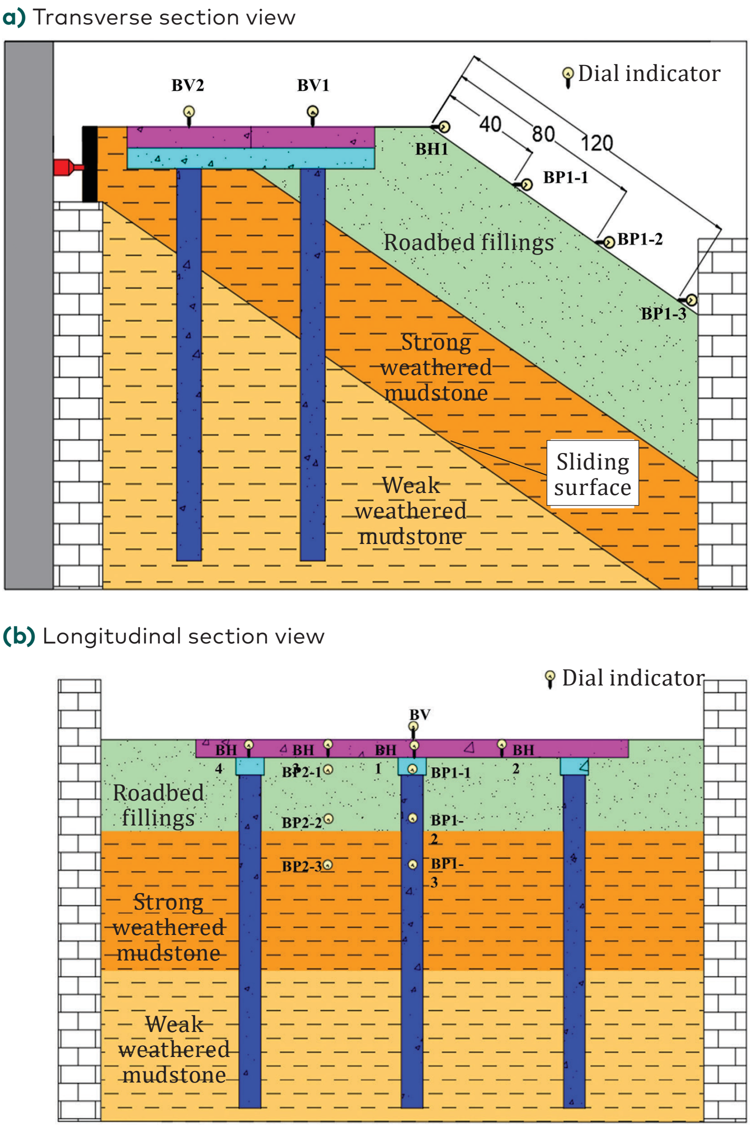

Figure 11. Displacement measuring point layout (unit: cm)

2.5. Loading program

To demonstrate the simulated effect of the remaining transmission of the sliding force, the layout of the loading device is shown in Figure 3. The test adopted the static pressure method to load step by step, and the hydraulic jack increased the horizontal load equivalent to 70 kN/m remaining sliding force for each step. The dial indicator reading was recorded every 5 min and the next portion of load was loaded after the data stabilized (in approximately 1 h). When a large displacement or deformation occurred on the surface of the roadbed and the next level of load could not be successfully loaded, the model could be considered broken, and the test completed. The specific loading classification is shown in Table 6.

Table 6. Load classification

Progression	1	2	3	4	5	6	7	8	9	10	11	12
Load, kN	0	14	28	43	57	71	86	100	114	129	143	157

3. Analysis of bearing characteristics

3.1. Stress distribution of the main reinforcement of the pile

Figures 12–15 demonstrate stress distribution of the main reinforcement of the pile when the load increased from zero to 157 kN. The stress of the steel bar linearly increased along with increasing load, indicating that the stress of the steel bar had not reached the stress limit state. In the following figures, the stress of the steel bar is positive in tension and negative in compression.

Figure 12 and Figure 13 show that the stress of pile reinforcement #1 increases along with increasing load. From the stress change trend, the steel bar of pile #1 is in tension above the sliding surface and in compression below the sliding surface. Although the data of pile #1 show a sudden change in some areas, the maximum tensile stress is slightly below 200 MPa, which does not reach the yield strength of the test steel bar. Therefore, pile body steel bars #1 are in the elastic working stage. The position of the maximum stress of pile body steel bar #1 is only 90 cm below the sliding surface and pile top, which is consistent with the position of pile body #1 where cracks are generated.

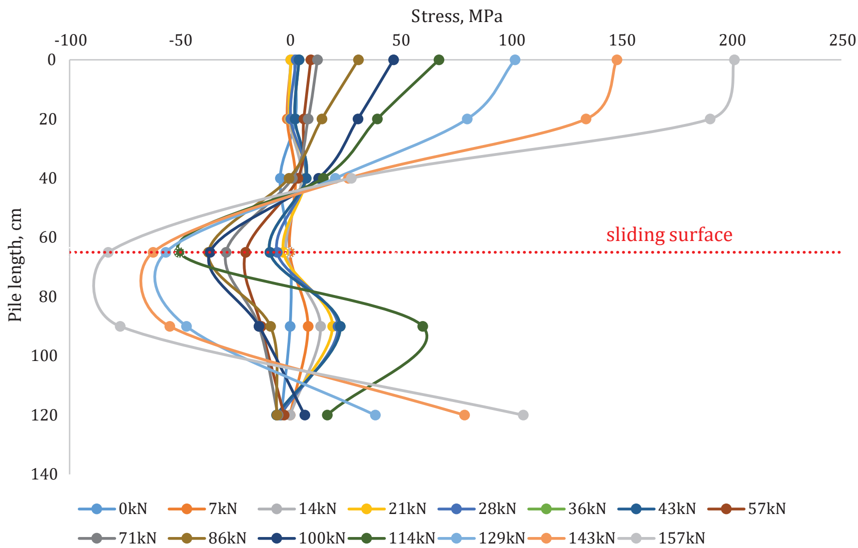

Figure 12. Stress distribution of the main reinforcement on the front side of pile #1

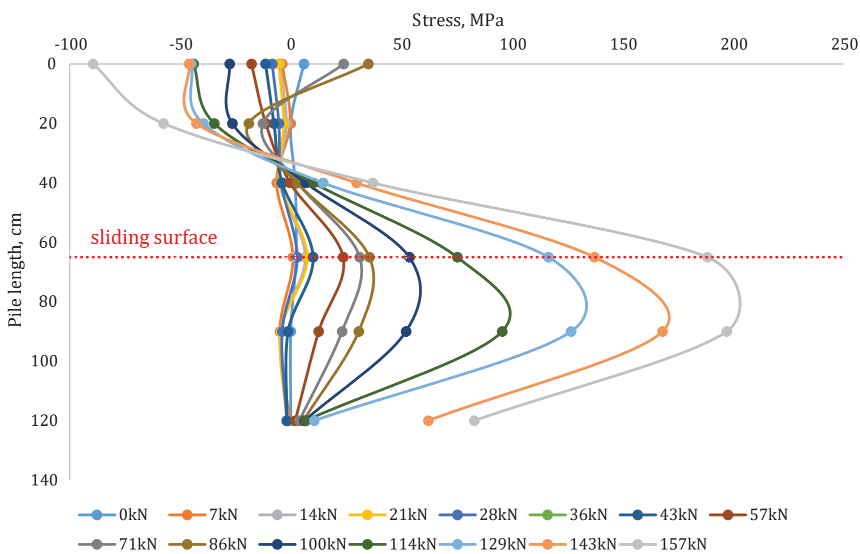

Figure 13. Stress distribution of the main reinforcement on the back side of pile #1

Figure 14 and Figure 15 show that the stress of the reinforcement in pile #2 increases along with the increase of the load, but when pile #2 is damaged, i.e., the load reaches 100 kN, part of the data demonstrates a decreasing trend. The steel bar of pile body #2 is basically in tension above the sliding surface and in compression below the sliding surface, which is basically identical to the force mode of pile #1.

When the load reaches 100 kN, the stress of the steel bar at pile top #2 and 60 cm below pile top #2 jumps. Simultaneously, the front side steel bar of pile #2 reaches a yield strength of 250 MPa, the back side steel bar of the pile reaches a yield strength of 280 MPa, and the pile body begins to break, which corresponds to the actual cracking position of pile #2.

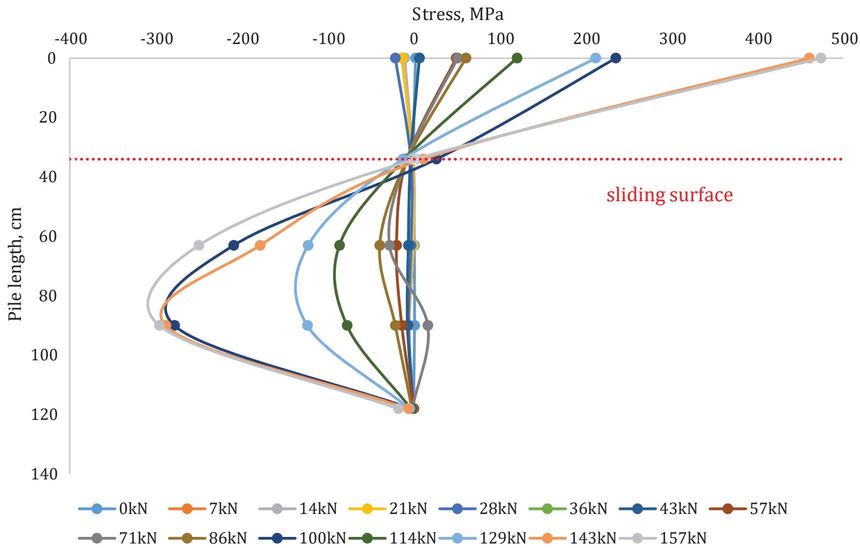

Figure 14. Stress distribution of the main reinforcement on the front side of pile #2

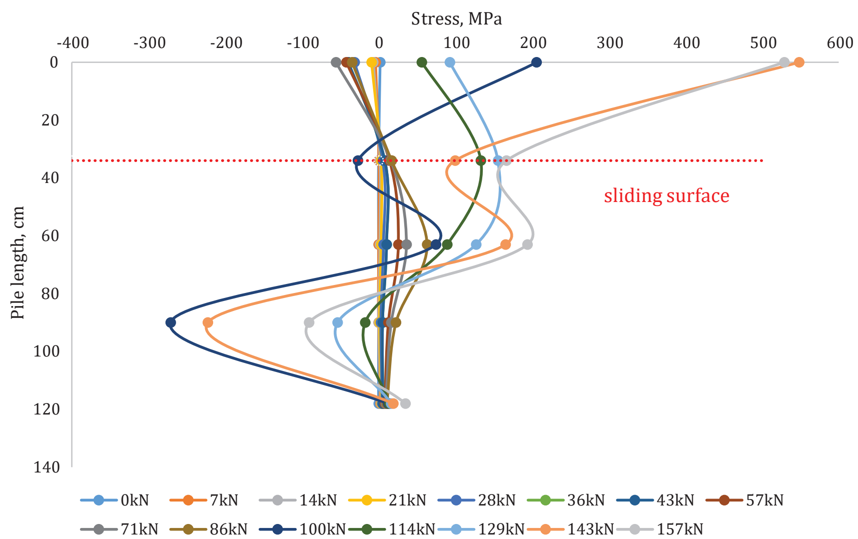

Figure 15. Stress distribution of the main reinforcement on the back side of pile #2

3.2. Analysis of the distribution law of earth pressure around piles

The earth pressure in front of the pile is the resistance force in front of the pile to the structure, which reflects the ability of the soil in front of the pile to resist structural deformation. However, the earth pressure behind the pile is an external load for the structure, which reflects the force that acts on the structure. The rigidity values of the pile and soil are inconsistent, which leads to voids between the pile and the soil. Therefore, the earth pressure cell must be set at a symmetrical position around the pile to test the horizontal earth pressure around the pile. The curves of earth pressure before and after the piles of piles #1 and #2 are shown in Figures 16–19.

Figure 16 and Figure 17 show that the distribution pattern of the soil pressure in front of pile #1 is close to a triangular shape. Above the sliding surface, the earth pressure in front of pile #1 is relatively large and gradually increases along with the increase of the load, which is caused by the pile body deformation and pile squeezing the soil in front of the pile. At a depth of 20 cm, the maximum earth pressure reaches 110 kPa. Below the sliding surface, the data remain stable at almost zero.

The distribution pattern of the earth pressure behind pile #1 is close to the R shape. The earth pressure is the largest at the sliding surface position and near the pile top. In addition, the earth pressure at the middle position is small and close to zero, which is conditioned by the separation between the soil and the pile. The maximum earth pressure at the sliding surface reaches 25 kPa and the maximum earth pressure at the top of the pile reaches 30 kPa.

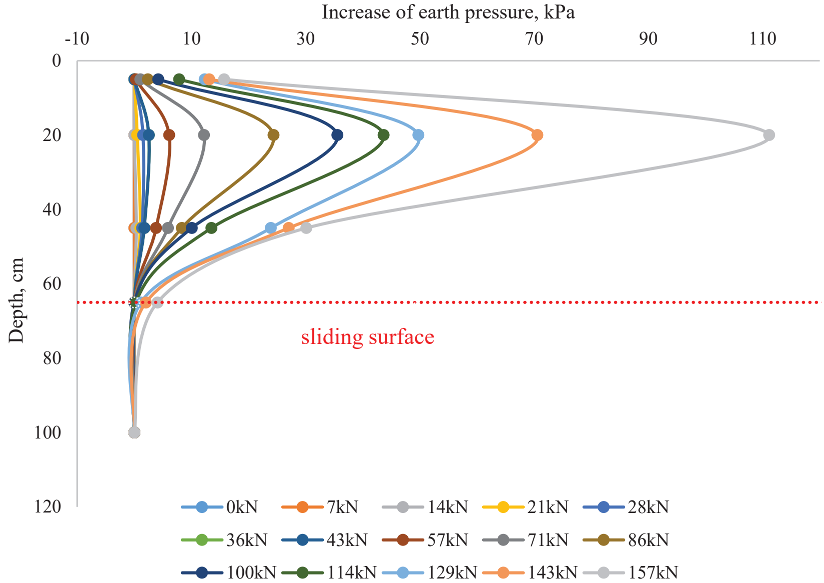

Figure 16. Increase of the earth pressure in front of pile #1

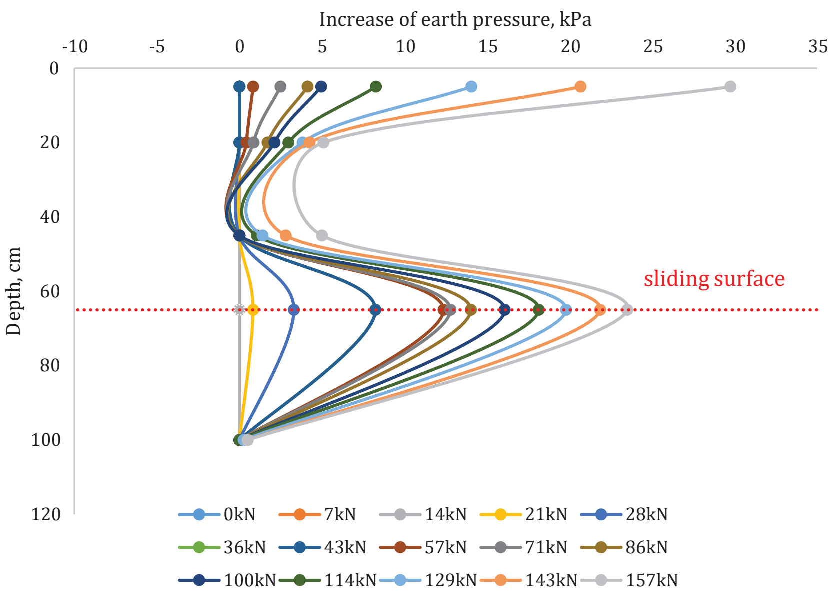

Figure 17. Increase of the earth pressure behind pile #1

Figure 18 and Figure 19 show that the distribution pattern of the earth pressure in front of pile #2 is close to a triangular shape. Above the sliding surface, the soil pressure in front of pile #2 remains unchanged at zero, which is caused by the void between the soil and the pile. Below the slip surface, the earth pressure in front of pile #2 is larger and gradually increases along with increasing load, which is caused by the deformation of the pile body and squeezing of the soil in front of the pile. The maximum earth pressure in front of pile #2 occurs at a depth of 60 cm; the maximum earth pressure reaches 85 kPa. Compared with the data of pile #1, the structural resistance force is mainly provided by the side soil pressure of pile #2.

In contrast, the distribution pattern of the earth pressure behind pile #2 is close to the R shape. Above the sliding surface, the earth pressure behind pile #2 gradually increases along with increasing load. At the position below the sliding surface, the earth pressure behind the back pile does not change with increasing load and basically remains at approximately 5 kPa. The maximum earth pressure behind pile #2 is near the top of the pile, the maximum earth pressure reaches 23 kPa.

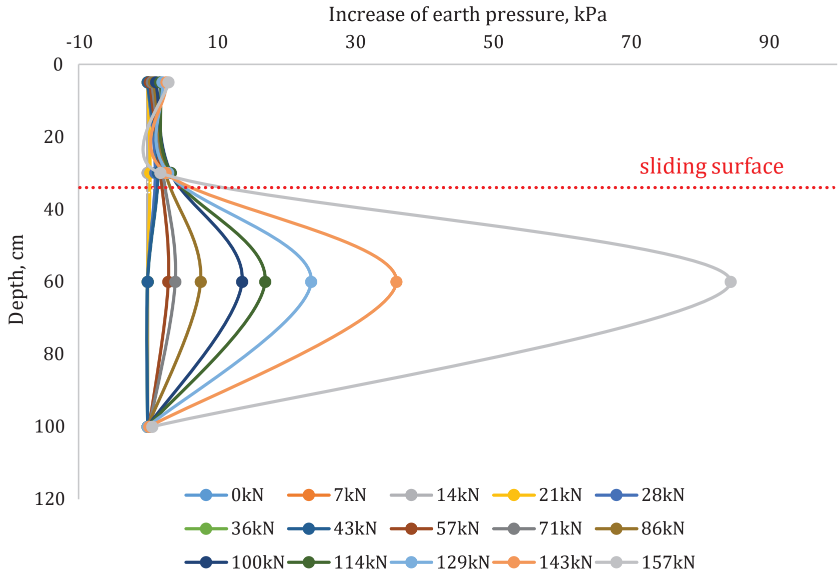

Figure 18. Increase of the earth pressure in front of pile #2

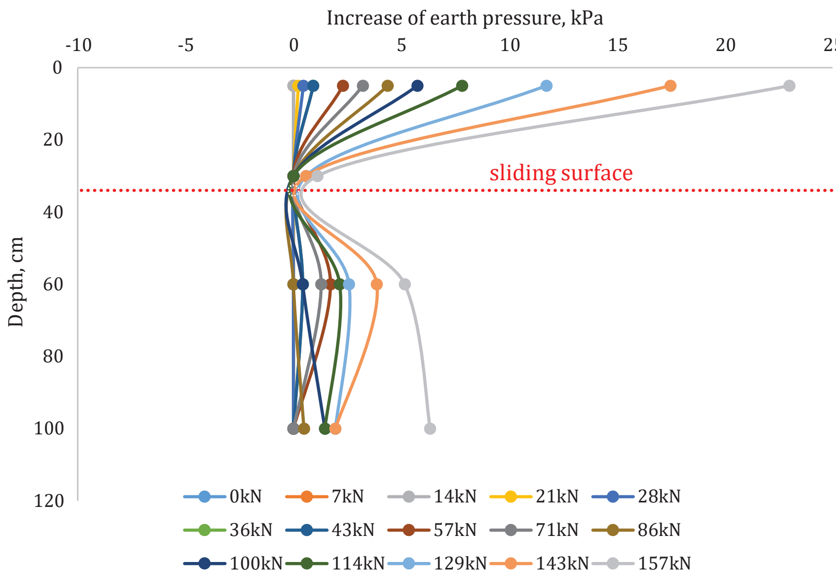

Figure 19. Increase of the earth pressure behind pile #2

3.3. Analysis of the displacement variation law of the bearing plate

The horizontal displacement of the bearing plate reflects the ability of the overall structure to resist horizontal external forces. The horizontal and vertical displacements of the bearing plate under an external load are shown in Figure 20 and Figure 21.

According to Figure 20, when the load increases to 143 kN, the horizontal displacement of the bearing plate increases significantly, and the slope surface has already undergone a large slip, indicating that the damage of the bearing plate begins. When the load increases to 157 kN, the maximum horizontal displacement of the bearing plate reaches 7.25 mm, which is equivalent to a displacement of 7.25 cm (similarity ratio 1:10) in the real life.

Figure 21 shows that when the load increases to 143 kN, the vertical displacement of the bearing plate increases significantly. When the load increases to 157 kN, the vertical displacement of the bearing plate BV1 is 0.7 mm and the vertical displacement of BV2 is 3.9 mm, the corresponding displacements in the real world are 0.7 cm and 3.9 cm, respectively. Considering also Figure 20 and Figure 21, it becomes evident that when the horizontal load reaches 143 kN, it is the turning point at which the structures changes from the normal bearing state to the failure bearing stage.

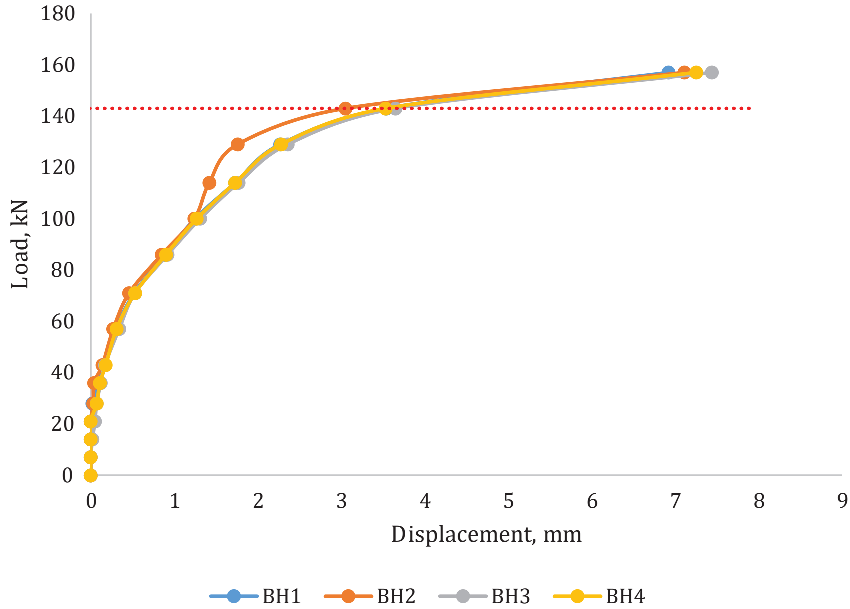

Figure 20. Horizontal displacement curve of the bearing plate

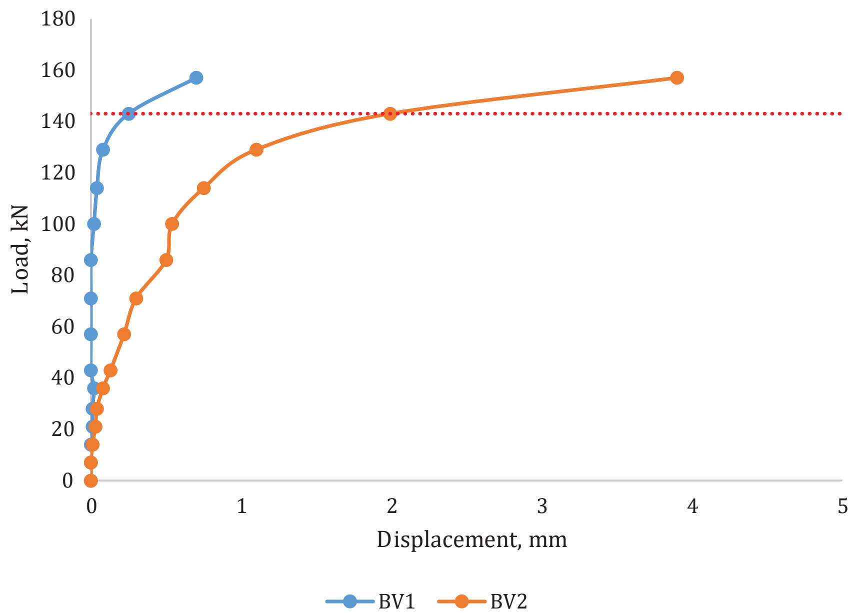

Figure 21. Vertical displacement curve of the bearing plate

3.4. Analysis of the displacement variation law of the slope

The horizontal displacement of the slope body reflects the deformation resistance of the structure. The deformation law of the slope body inder the action of an external load is shown in Figure 22 and Figure 23.

Figure 22 and Figure 23 show that when the load is less than 57 kN, the slope surface displacement is 0, and part of the displacement is negative due to the slight slip between the dial gauge needle and the displacement measuring point gasket during the test. Therefore, the slope body does not deform. When the load increases to 57 kN, the slope begins to move outward; when the load is increased, the horizontal displacement of the slope gradually increases.

Figure 22 shows that the maximum horizontal displacement of the measuring point (BP1-1) 40 cm from the top of the slope is 5.84 mm, the maximum horizontal displacement of the measuring point (BP1-2) 80 cm from the top of the slope is 2.68 mm, and the maximum horizontal displacement of the measuring point (BP1-3) 120 cm from the top of the slope is 1.35 mm. Closer to the top of the slope, the horizontal displacement of the slope body increases. Moreover, the horizontal displacement of the slope presents an inverted triangle form.

Figure 23 shows that the maximum horizontal displacement of the measuring point (BP2-1) 40 cm from the top of the slope is 6.02 mm, the maximum horizontal displacement of the measuring point (BP2-2) 80 cm from the top of the slope is 2.56 mm, and the maximum horizontal displacement of the measuring point (BP2-3) 120 cm from the top of the slope is 2.16 mm.

A comparison of Figure 22 and Figure 23 shows the horizontal displacement of different sections and indicates that the same height measurement point is less different at only 2.9%. Thus, the force transferred from the structure to the subgrade filling material from different sections is relatively uniform and the slope will not produce uneven deformation along the train running direction.

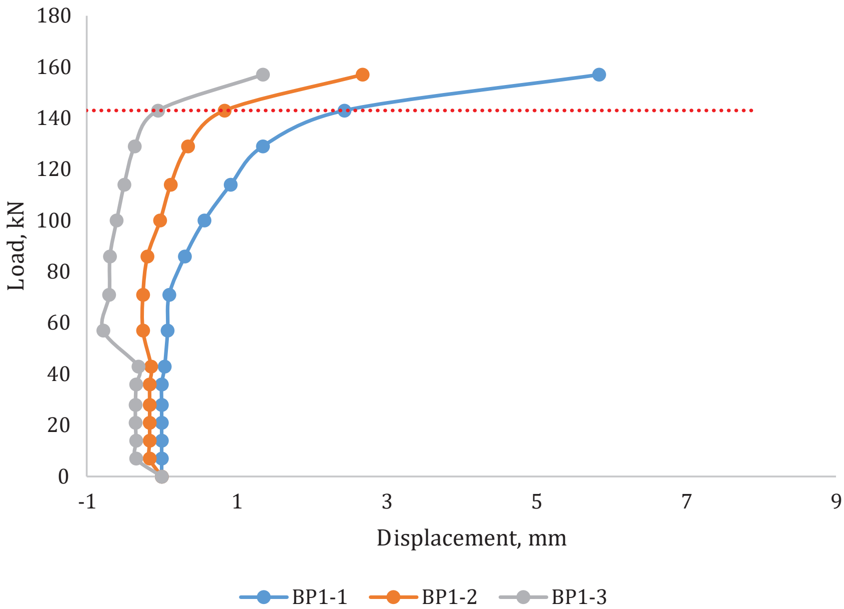

Figure 22. Slope displacement of the cross-section of pile foundation

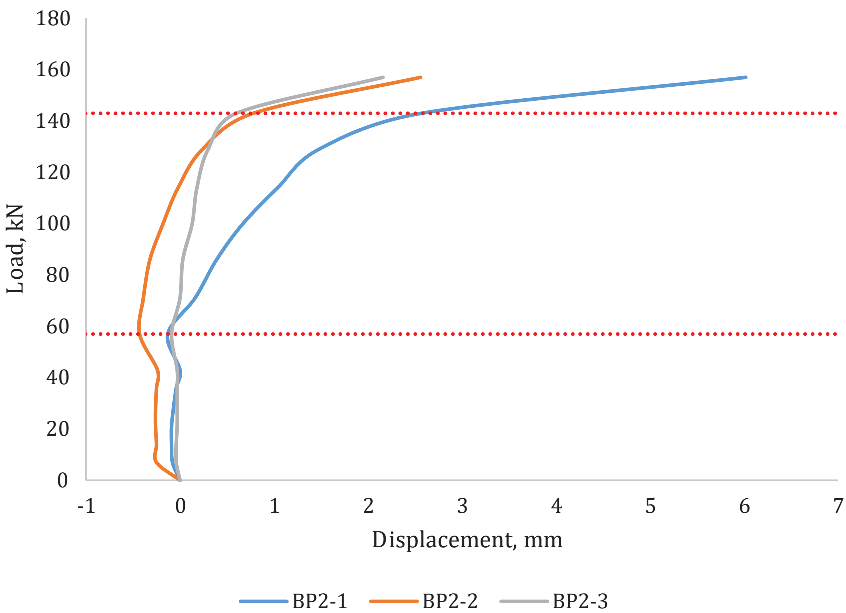

Figure 23. Slope displacement of the interrupted surface

4. Failure characteristics

4.1. Slope and bedrock

The roadbed slope begins to deform when the horizontal load reaches 57 kN. When loaded to 157 kN, the slope experiences a significant shallow damage and local collapse (Figure 24). The contact position between the pile and the bedrock exhibits obvious compression and uplift (Figure 25). At this moment, it is equivalent to the remaining sliding force in the actual project reaching 770 kN/m (equivalent to the slope length of 79.123 m), which indicates that this type of pile-slab structure roadbed demonstrates good resistance to deformation.

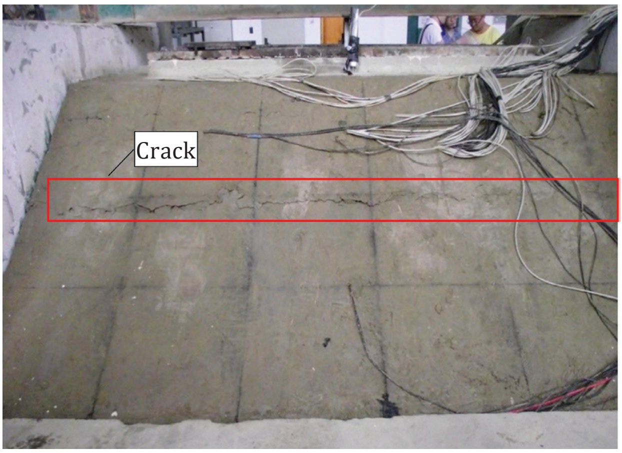

Figure 24. Slope surface deformation

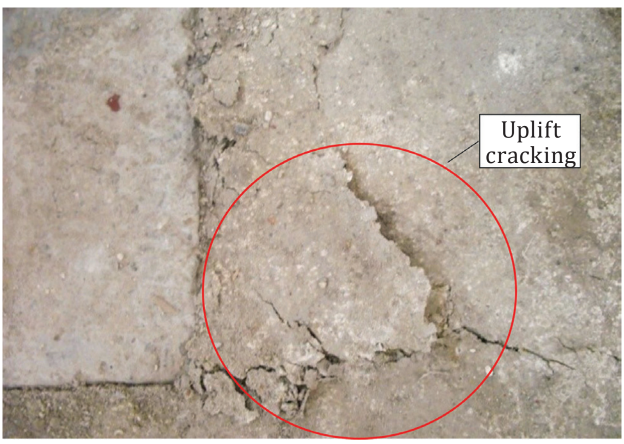

Figure 25. Uplift and cracking of the bedrock

4.2. Structural failure characteristics

After the structure was excavated, there were obvious cracks on pile #1 and pile #2. The cracks were mainly located near the top of the pile and the sliding surface (Figure 26). The piles between the cracks were tilted, and no damage was observed. The remaining piles remained intact and basically vertical. Due to the relative deformation of the pile and soil, pile-soil voids appeared near the sliding surface and behind the pile body at the top of the pile.

Combined with the law of the stress change of the steel bar, the steel bar exhibits a stress concentration phenomenon at the top of the pile and at the damage of the pile body because after the concrete cracks, the tensile stress it bears is transferred to the steel bar, which causes a sharp increase in stress of the steel bar.

Considering the failure mode, when the load increases from zero to 100 kN, the steel bars on the back side of the pile yield first. Then, the bars on the front side of the pile enter a yielding state. Simultaneously,

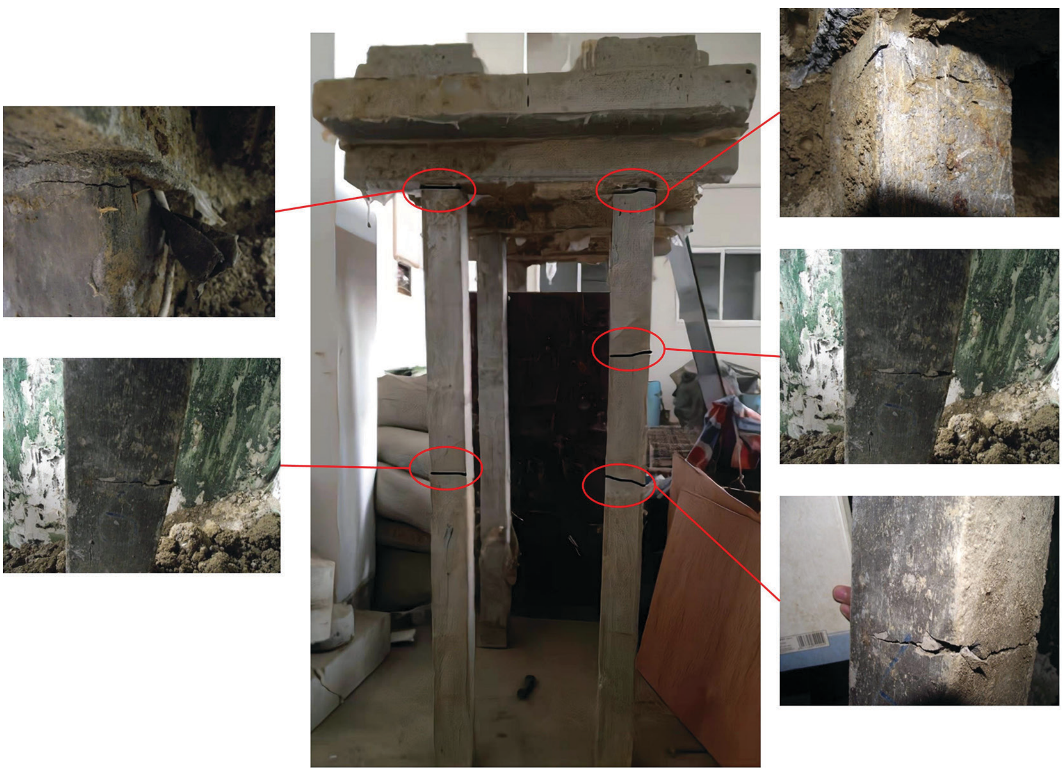

Figure 26. Structural destruction diagram

the pile fractures at the sliding surface. As time passes and the load increases, new cracks appear below the fracture point, which are located approximately 43 cm below the slip surface. The pile-slab structure is subjected to landslide thrust and the pile slopes toward the leading edge of the landslide. Due to the long anchorage depth of the pile slab structure, the pile body near the base of the pile is basically not deformed. The specific location of the crack distribution is shown in Figure 27.

In summary, the damaged part of the pile-slab structure is located near the sliding surface and pile top. The top of pile #2 fails during bending due to landslides, and tensile cracks are generated. The top of pile #1 produces tensile cracks due to the action of the soil between the piles. The anchored pile body is damaged by bending 9 cm below the sliding surface, and tensile cracks occur in the pile body.

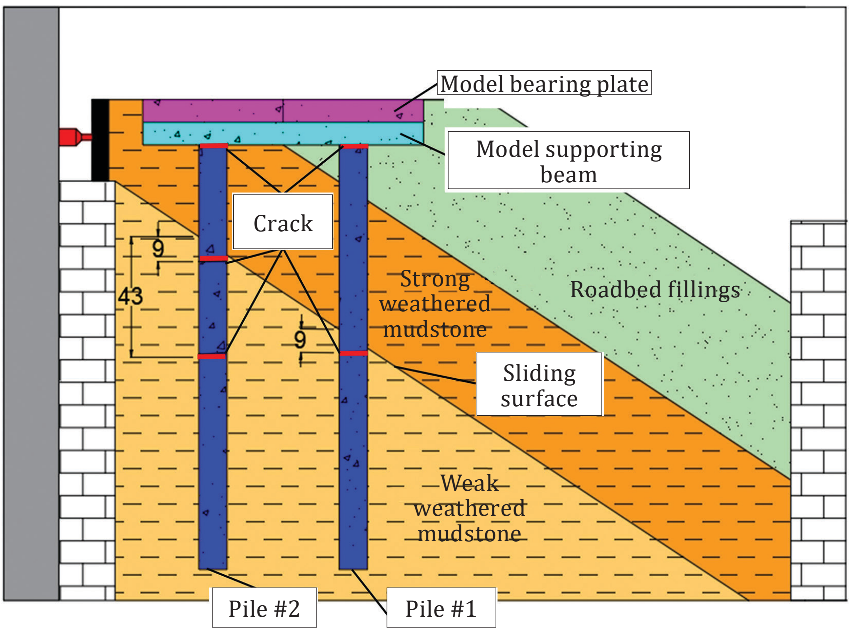

Figure 27. Crack distribution position (unit: cm)

5. Validation of the model test

Landslide thrust of the test-simulated section was calculated using the transfer coefficient method (TB10025-2006). The calculated result is 570 kN/m, which is equivalent to the 9-level load in the model test, and then the combined force of soil pressure applied to the post-pile is equally distributed to the structure. The structural mechanical displacement method (Long, 2017) was used to calculate the internal forces of the pile-slab structure; the structural force analysis is shown in Figure 28. p_1 is the overlying load of the structure, p_2 is the smaller of the remaining slip resistance, passive earth pressure and elastic resistance of the front pile, p_3 is the soil pressure on the back side of the front pile, p_4 is the soil pressure on the front side of the rear pile, p_5 is the slope thrust of the rear pile, l_0 is the length of section DF and AB, r is the length of section BD, h_2 is the length of section DE, and h_3 is the length of section BC.

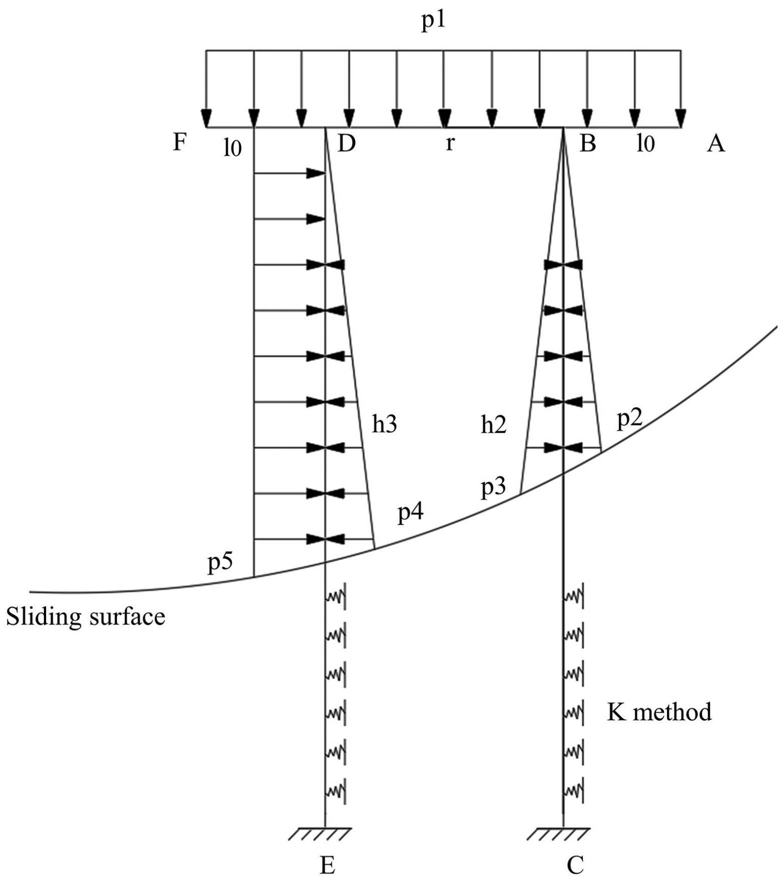

Figure 28. Structural force diagram

Taking BD as the isolator, the equilibrium equation is established and the solution matrix is obtained, as shown in Equation (5).

$$\begin{pmatrix} 4(i_{BC}+i_{BD}) & 2i_{BD} & -\dfrac{6i_{BC}}{h_2} \\ 2i_{BD} & 4(i_{BC}+i_{BD}) & -\dfrac{6i_{DE}}{h_3} \\ -\dfrac{6i_{BC}}{h_2} & -\dfrac{6i_{DE}}{h_3} & 12\left(\dfrac{i_{BC}}{h_2{}^2}+\dfrac{i_{DE}}{h_3{}^2}\right) \end{pmatrix} \begin{pmatrix} \theta_B \\ \theta_D \\ \Delta \end{pmatrix} = \begin{pmatrix} \dfrac{1}{30}(p_3-p_2)h_2^2+\dfrac{1}{12}p_1r^2-\dfrac{1}{2}p_1l_0^2 \\ \dfrac{1}{12}p_5h_3^2-\dfrac{1}{12}p_1r^2-\dfrac{1}{30}p_4h_3^2-\dfrac{1}{2}p_1l_0^2 \\ -\dfrac{1}{6}(p_3-p_2)h_2+\dfrac{1}{6}p_4h_3-\dfrac{1}{2}p_5h_3 \end{pmatrix} \quad (5)$$

According to Equation (5) θ_B, θ_D, Δ can be solved, and thus the equation of internal force of the structure can be obtained.

The bending moment and shear force of any section of the front pile in the double-row pile plate structure are positive in clockwise direction, and the axial force is positive in tension. With point *B* as the base point, the graph moves downward as the positive y-axis and to the right as the positive x-axis. The formula for calculating the internal force of the front pile is shown in Equation (6). The formula for calculating the internal force of the rear pile is shown in Equation (7). The structural reaction force below the sliding surface is determined by the K method (TB10025-2006).

$$M_y=-4i_{BC}\theta_B+\frac{6i_{BC}\theta_B y}{h_2}+\frac{6i_{BC}\Delta}{h_2}-\frac{12i_{BC}\Delta y}{h_2^2}+\frac{(p_3-p_2)h_2^2}{30}+\frac{(p_3-p_2)y^3}{6h_2}-\frac{3(p_3-p_2)h_2 y}{20} \quad (6)$$

$$M_y=-4i_{DE}\theta_D+\frac{6i_{DE}\theta_D y}{h_3}+\frac{6i_{DE}\Delta}{h_3}-\frac{12i_{DE}\Delta y}{h_3^2}-\frac{p_4h_3^2}{30}-\frac{p_4y^3}{6h_3}+\frac{3p_4h_3 y}{20}+\frac{p_5h_3^2}{12}+\frac{p_5y^2}{2}-\frac{p_5h_3 y}{2} \quad (7)$$

The test results of the model test under Level 9 load were compared with the above-presented theoretical calculations, as shown in Figure 29.

Comparing the empirical test results with the results of theoretical calculations, both appear to be subject to the same variation law. They also demonstrate close values, so empirical test results have been considered to have a high degree of reliability.

Conclusion

In this study, large-scale failure tests of pile-slab structure were conducted to investigate the bearing performance and failure characteristics of pile-slab structures. The change laws of stress and displacement of pile-slab structures in steep slopes have been clarified, the damage process and failure characteristics of pile-slab structure have been discussed. The following conclusions have been drawn.

a) pile #1

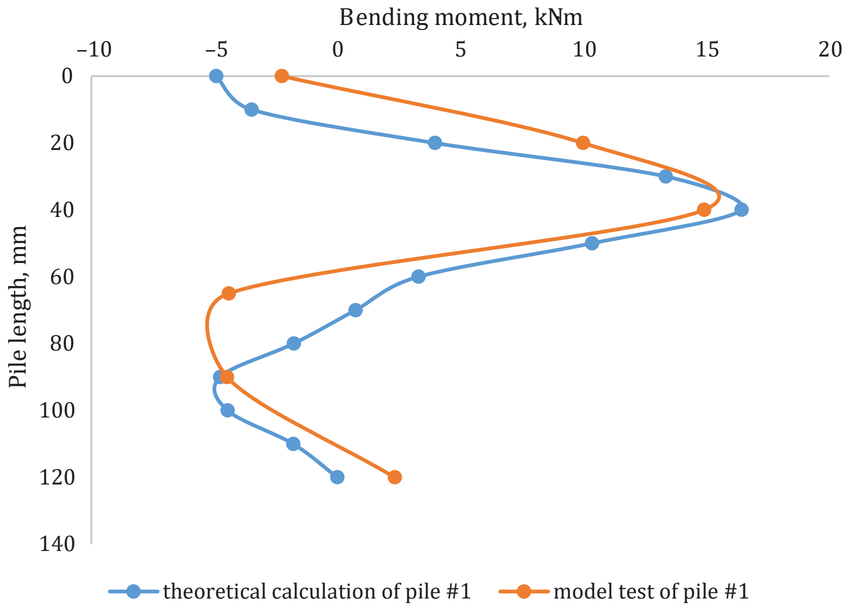

b) pile #2

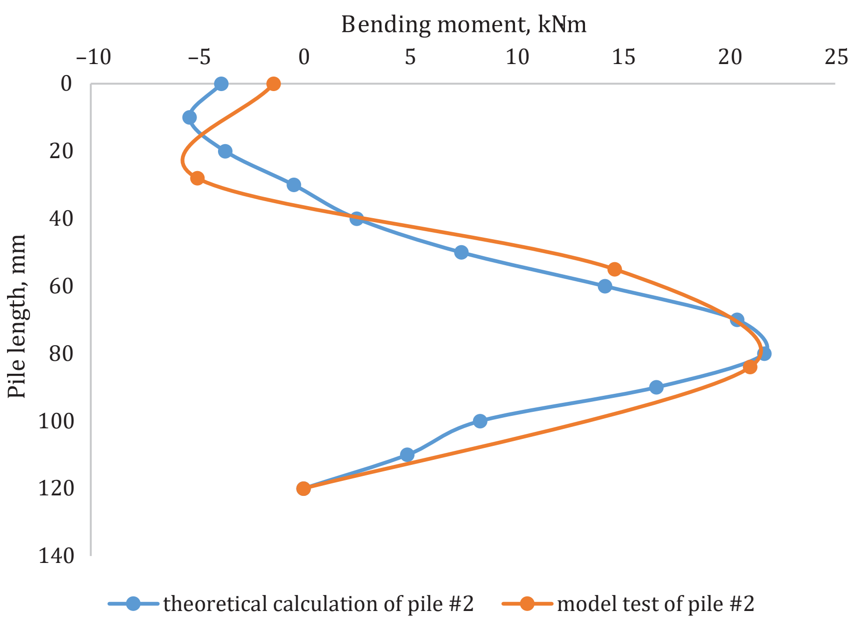

Figure 29. Comparison of experimental and theoretical results

1. During the loading process within the test, the outer pile (pile #1) was always in the elastic deformation stage. When the horizontal load was increased to 100 kN, the inner pile (pile #2) exhibited a yield failure. In other words, the maximum horizontal load that the inner pile (pile #2) can bear is 100 kN, and pile #1 has a higher bearing capacity than the inner pile (pile #2). Therefore, the engineering design should focus on the inspection of the bearing capacity of the inner pile (pile #2).
2. The working stages of the pile-slab structure roadbed in steep slopes can be roughly divided into three phases: the precracking stage, the working stage with cracks and the steel bar yield stage. The two typical characteristics demonstrated by the piles are transverse cracking and diagonal cracking during the loading process.
3. The cracks in the pile body are mainly located near the top of the pile and near the sliding surface of the anchoring section. Therefore, in engineering design, it is necessary to pay attention to calculating and predicting the location of structural cracks and take corresponding engineering measures to control the cracks.
4. In the failure test, when the remaining sliding force of the prototype slope reached 770 kN/m (equivalent to a slope length of 79.123 m), the structure was destroyed. Therefore, sections with remaining slipping forces greater than 770 kN/m should be cautiously adopted for such subgrade support structures.
5. When the structure is damaged, the maximum horizontal displacement of the bearing plate reaches 7.25 mm. The maximum vertical displacement of the inner side of the bearing plate is 3.9 mm, and the value of inner lifting is 5.6 times the value of outer lifting. The bearing plate swells and rises on the loading side, and the double-row pile-slab structure rotates slightly.
6. When the structure is damaged, the deformation of the structure is 1.5 times the deformation of the slope. With regard to the degree of damage, the structural damage exceeds the slope damage, which may consider to be beneficial for the designer since it would allow controlling the overall stability of the slope.

Funding

This work was supported by the National Natural Science Foundation of China under Grant [number 51978588].

REFERENCES

ASTM. (2018). *C39/39M-18 standard test method for compressive strength of cylindrical concrete specimens*. ASTM International: West Conshohocken, PA, USA.

Buslov, A., & Margolin, V. (2018). The influence of the second row of piles in double-row pile retaining walls with the stabilization of landslide. *21st International Scientific Conference on Advanced in Civil Engineering Construction – The Formation of Living Environment*, *365*(5), Article 052006. http://doi.org/10.1088/1757-899X/365/5/052006

Buslov, A., & Margolin, V. (2017). The interaction of piles in double-row pile retaining walls in the stabilization of the subgrade. *19th International Scientific Conference on Energy Management of Municipal Transportation Facilities and Transport*, *692*, 769–775. http://doi.org/ 10.1007/978-3-319-70987-1_81

Chau, C., Soga, K., O'Riordan, N., & Nicholson, D. (2012). Embodied energy evaluation for sections of the UK Channel Tunnel rail link. *Proceedings of the Institution of Civil Engineers – Geotechnical Engineering*, *165*(2), 65–81. http://doi.org/10.1680/geng.9.00018

Di Laora, R., Maiorano, R. M. S., & Aversa, S. (2017). Ultimate lateral load of slope-stabilising piles. *Géotechnique Letters*, *7*(3), 237–244. http://doi.org/10.1680/jgele.17.00038

Fan, G., Zhang, J. J., & Qi, S. C. (2019). Dynamic response of a slope reinforced by double-row antisliding piles and pre-stressed anchor cables. *Journal of Mountain Science*, *16*(1), 226–241. http://doi.org/10.1007/s11629-018-5041-z

Gao, X. H., Tian, W. P., & Zhang, Z. P. (2020). Simulation parameter test and seepage effect analysis of pile-anchor support for binary slope. *Advances in Civil Engineering*, *2020*, Article 8862163. http://doi.org/10.1155/2020/8862163

Guo, Y. C., Du, H., & Li, Y. H. (2019). Stability analysis and application of two-stage support on the high fill slope. *International Conference on Computer Information Science and Application Technology, 1168*(2), Article 022064. http://doi.org/10.1088/1742-6596/1168/2/022064

Galli, A., & di Prisco, C. (2013). Displacement-based design procedure for slope-stabilizing piles. *Canadian Geotechnical Journal*, *50*(1), 41–53. http://doi.org/10.1139/cgj-2012-0104

China Planning Press. (2019). *GB/T 50123-2019: Standard for Geotechnical Test Methods*.

China Railway Press. (2006). *TB10025-2006, Specification for design of railway subgrade support structure*.

Huang, J. J., Su, Q., & Liu, T. (2015). Vibration and long-term performance analysis of pile-plank-supported low subgrade of ballastless track under excitation loads. *Shock and Vibration*, *2015*, Article 404627. http://doi.org/10.1155/2015/404627

Jiang, Y., Han, J., & Zheng, G. (2014). Numerical analysis of a pile-slab-supported railway embankment. *Acta Geotechnica*, *9*(3), 499–511. http://doi.org/10.1007/s11440-013-0285-9

Kahyaoglu, M. R., Imanch, G., & Ozden, G. (2017). Numerical simulations of landslide-stabilizing piles: a remediation project in Soke, Turkey. *Environmental Earth Sciences*, *76*, Article 656. http://doi.org/10.1007/s12665-017-6989-7

Li, S. L., Wei, L. M., & Chen, X. B. (2020a). Numerical investigation on dynamic performance of a bridge-tunnel transition section with a deep buried pile-plank structure. *Advances in Civil Engineering*, *2020*, Article 8885535. http://doi.org/10.1155/2020/8885535

Li, C. D., Chen, W. Q., & Song, Y. J. (2020b). Optimal location of piles in stabilizing slopes based on a simplified double-row piles model. *KSCE Journal of Civil Engineering*, *24*(2), 377–389. http://doi.org/10.1007/s12205-020-0712-z

Lei, H. Y., Liu, X., & Song, Y. J. (2021). Stability analysis of slope reinforced by double-row stabilizing piles with different locations. *Natural Hazards*, *106*, 19–42. http://doi.org/10.1007/s11069-020-04446-2

Long Yuqiu. (2017). *Structural mechanics* (3rd ed.). Higher Education Press, Bei Jing, China.

Messioud, S., Okyay, U. S., & Sbartai, B. (2016). Dynamic response of pile reinforced soils and piled foundations. *Geotechnical and Geological Engineering*, *34*(3), 789–805. http://doi.org/10.1007/s10706-016-0003-0

Messioud, S., Sbartai, B., & Dias, D. (2017). Estimation of dynamic impedance of the soil-pile-slab and soil-pile-mattress-slab systems. *International Journal of Structural Stability and Dynamics*, *17*(6), Article 1750057. http://doi.org/10.1142/S0219455417500572

Ravera, E., Sutman, M., & Laloui, L. (2020). Analysis of the interaction factor method for energy pile groups with slab. *Computers and Geotechnics*, *119*, Article 103294. http://doi.org/10.1016/j.compgeo.2019.103294

Troncone, A., Pugliese, L., Lamanna, G., & Conte, E. (2021). Prediction of rainfall-induced landslide movements in the presence of stabilizing piles. *Engineering Geology*, *288*, Article 106143. http://doi.org/10.1016/j.enggeo.2021.106143

Wei, L. M., Li, S. L., & Lin, Y. L. (2020). Dynamic performance of a deep buried pile-plank structure transition section for a high-speed railway – Field tests and numerical analyses. *Transportation Geotechnics*, *25*, Article 100408. http://doi.org/10.1016/j.trgeo.2020.100408

Wang, Z., Yu, Y., & Sun, H. Y. (2020). Robust optimization of the constructional time delay in the design of double-row stabilizing piles. *Bulletin of Engineering Geology and The Environment*, *79*(1), 53–67. http://doi.org/10.1007/s10064-019-01554-7

Xiao, S. G., Zeng, J. X., & Yan, Y. P. (2017). A rational layout of double-row stabilizing piles for large-scale landslide control. *Bulletin of Engineering Geology and The Environment*, *76*(1), 309–321. http://doi.org/10.1007/s10064-016-0852-z

Xie, Q., Cao, Z. L., & Shi, X. K. (2021). Model test of interaction between load-caused landslide and double-row anti-slide piles by transparent soil material. *Arabian Journal for Science and Engineering, 46*, 4841–4856. http://doi.org/10.1007/s13369-020-05256-1

Xv, T. (1982). *Similarity theory and model experiments*. China Agricultural Machinery Press, Bei Jing, China.

Zhang, D. B., Zhang, Y., & Kim, C. W. (2018). Effectiveness of CFG pile-slab structure on soft soil for supporting high-speed railway embankment. *Soils and Foundations*, *58*(6), 1458–1475. http://doi.org/10.1016/j.sandf.2018.08.007

Zhou, Y. J., Liu, K. M., & Wang, F. N. (2021). Research on the mechanical properties of new double-row pile supporting structure based on an in situ study. *Shock and Vibration*, *2021*, Article 5177777. http://doi.org/10.1155/2021/5177777

Zhu, Y. P., Wei, Z. H., & Zhu, Q. H. (2020). Application research of a prestressed anchor cable-pile-slab wall supporting structure for multistage high fill slopes. *Engineering Reports, 2*(2), Article e12120. http://doi.org/10.1002/eng2.12120

Zhou, Y. J., Yao, A. J., & Zheng, X. (2016). A model test study of double-row piles in deep foundation pit excavation. *Electronic Journal of Geotechnical Engineering*, *21*(4), 1701–1714.